HTML ABSTRACT + LINKS

Realization of nanoscale resolution with a micromachined thermally actuated testing stage

Shaoning Lu, Dmitriy A. Dikin, Sulin Zhang, Frank T. Fisher, Junghoon Lee, and Rodney S. Ruoff[a]

Department of Mechanical Engineering, Northwestern University, Evanston, Illinois 60208-3111

(Received 1 December 2003; accepted 19 January 2004; published online 24 May 2004)

The design, fabrication, and characterization of a microelectromechanical systems (MEMS) stress–strain device for testing the mechanical properties of nanomaterials is presented. Thermal actuation, with integrated motion amplification structures, was used to both minimize the operating temperature of the device as well as realize fine motion control over large displacements. The device has a working range from tens of nanometers up to 10 micrometers. Displacements as small as 30 nm per 10 mA input dc current increments were obtained for the first time with thermal actuators micromachined by deep reactive ion etching (DRIE). The height difference (offset) between the moving and fixed platforms was less than 40 nm over the entire working range of the device for the input power range studied. A 0.27 μN force is predicted for an actuator displacement of 30 nm based on mechanical models of the device; the calculated force increases linearly up to 88 μN for the maximum 9.7 μm displacement. The operating characteristics obtained for this initial design suggest that this methodology will be useful in producing a variety of MEMS stress–strain stages custom designed to yield the force and displacement resolution necessary to test many nanomaterials and nanostructures. © *2004 American Institute of Physics.*
[DOI: 10.1063/1.1710703]

I. INTRODUCTION

While experimental measurement of the mechanical properties of nanostructures (including nanoscale wires, fibers, tubes, plates, and thin films) is a challenging endeavor, recent progress has been made in this area. For example, nanomanipulation and tensile testing of single walled carbon nanotube (SWCNT) ropes and individual multiwalled carbon nanotubes have been done inside a scanning electron microscope (SEM) with a nanomanipulator having piezoelectric actuated components.[1–4] Very long nanotube ropes (~2 mm) have been stressed with a large puller designed for samples longer than 1 mm.[5] Microelectromechanical systems (MEMS) offer a promising class of very small actuators and diagnostic tools for stressing nanostructures under various mechanical and electromechanical loading conditions. MEMS also provide the potential for mass fabrication of testing stages for high throughput and standardized testing, similar to disposable lab-on-chip products. However, there is the challenge of achieving high-resolution nanoscale control using MEMS.

We report the use of silicon microfabrication techniques to produce an integrated silicon chip with self-actuation based on thermal expansion. The device yields nanoscale displacement resolution, and through indirect force-sensing elements can be used for load-deformation studies of nanomaterials and nanostructures. This MEMS testing stage is significantly smaller than many other currently available manipulators, such as the two types of manipulators used in Refs. 1–5. The device was designed to accommodate many different nanostructures, such as carbon nanotubes, various types of nanowires, or thin planar films or platelets. Because of its size, it is also a candidate for use in the more highly constrained transmission electron microscope (TEM) environment.

Several efforts have been made to fabricate nano- or micropositioners using MEMS. By using various surface and bulk micromachining technologies, pioneering results have been obtained by using microfabricated cantilevers integrated with scanning probe tips. Actuation on the order of a few hundred nanometers has been obtained by electrostatically actuated $x-y$ translators combined with electron-beam (e-beam) lithography.[6,7] However, for mechanical loading of nanoscale structures, such as CNTs, a relatively large force output is required in conjunction with controlled displacements at the nanometer level. Sufficient electrostatic forces would require very large devices or very high driving voltages.[8] Moreover, e-beam lithography has very low yield, compared to the photolithography used here. We can readily put more than 100 devices on a 4 in. wafer during one lithography process. While micromachined structures have been used as platforms for mounting nanotubes, they rely on separate piezodrives/motors to provide the proper force and displacement;[9,10] the total size of these devices is much larger than could be achieved with a fully integrated self-actuated MEMS device.

As an alternative to electrostatic actuation, thermal actuator is an excellent transducer of strain to displacement[11–15] and can provide a much larger output force per unit device size when compared to an electrostatic actuator.

[a]Author to whom correspondence should be addressed; electronic mail: r-ruoff@northwestern.edu

 © 2004 American Institute of Physics

Downloaded 04 Jun 2004 to 129.105.90.23. Redistribution subject to AIP license or copyright, see http://rsi.aip.org/rsi/copyright.jsp

Different thermal actuators have been built using a variety of designs.[16–18] To date, the primary limitation of such devices is that motion resolution on the order of tens of nanometers has not been achieved. However, in the current work, we have used bent beam (V-beam) amplification structures that are capable of covering a relatively large range of displacements—from nanometers to micrometers. In this case, thermal expansion caused by a relatively small temperature increase results in a large displacement of the actuated structure.[11,13] Nanoscale displacement is based on a small temperature change (~ 1 °C) in the actuator, such small operating temperatures also reduce the amount of heat conduction to the sample area. Our actuator design also prohibits current flowing through the sample being tested. Thus, our approach minimizes the influence of the thermally actuated test device on the mechanics of the nanostructure.

First, we describe the design and fabrication of the device using deep reactive ion etching (DRIE). The methods used to characterize the device and its operational behavior, and the results obtained for the current device, are then described. We measured ~ 30 nm displacement per 10 mA current change (equivalent to 2.5 mW power input) in a vacuum (inside a SEM), by using a newly developed method of motion measurement obtained by capturing an instantaneous image shift, as described further below. We found that the fixed and movable platforms, separated by a 20 μm gap at rest, open to a gap as large as 30 μm while remaining essentially coplanar (a maximum vertical offset of 40 nm over the full range of actuation was observed with the use of an optical profilometer). Analytic and numerical solutions using standard beam mechanics show that the force range of the device is from 0.27 μN to 88 μN.

II. PRINCIPLE, DESIGN, AND FABRICATION

Our testing stages were designed and fabricated to provide a controlled gap size with the capability of measuring displacement and force by SEM imaging while mechanically loading a nanostructure. As shown in Fig. 1(a), the device consists of two separate and suspended parts, a moving structure (upper part of image) and a fixed structure (lower part of image). Each suspended part in the device has a platform with a narrow tip (the tip shape can be changed if necessary) extending outward and creating a controlled gap, which was 20 μm wide for the device shown here. The moving platform moves along the axis of the gap [Fig. 1(c)] so that the size of the gap can be controlled during actuation. The test specimen is prepared separately and placed across the opposing platforms, spanning the gap. The ends of the nanostructure can be clamped to the top surface of each platform using techniques such as electron-beam-induced decomposition,[1–4] or by simply taking advantage of van der Waals or other adhesive interactions. After careful characterization of the stand-alone device (with no test specimen present), the change in the device characteristics due to the presence of the nanostructure test specimen will yield the mechanical behavior of the nanoscale samples.

The electrothermal actuator consists of two pairs of thermal expansion beams and a narrow V-shaped compliant displacement amplifier (V-beam), symmetrically arranged around the center line, as shown in Fig. 1(a). Another thin beam attached to the fixed platform and connected to the moving platform at its center is used as a force-sensing element [Fig. 1(a)]. These structures are suspended over the substrate and connected to large silicon pads, which we refer to as the silicon electrodes. Electrical (gold) contact pads are

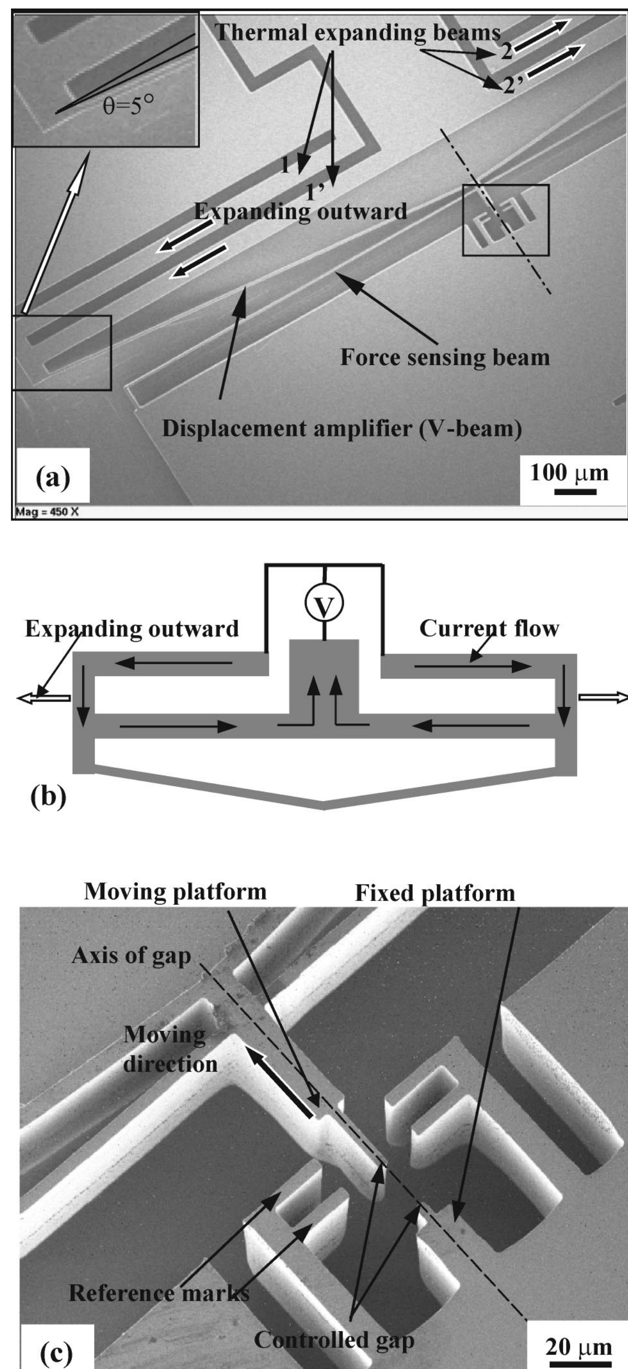

FIG. 1. (a) SEM (Hitachi S-4500) image of the device. The thermal expansion beams 1-1′ and 2-2′, indicated by the arrows, are symmetric relative to the center line (dashed line) of the device. Beams 1 and 2 are 970 μm long, while beams 1′ and 2′ are 1000 μm long. The width of the beams is 50 μm. The thickness of the device Si layer is 130 μm. The upper left-hand side inset is a higher magnification image of the connection between the thermal expansion beams and V-shaped beams. (b) The current flow during actuation. (c) The magnified central gap region.

Downloaded 04 Jun 2004 to 129.105.90.23. Redistribution subject to AIP license or copyright, see http://rsi.aip.org/rsi/copyright.jsp

patterned on top of the silicon electrodes, which are anchored to the underlying silicon base (not shown in Fig. 1). The electrodes provide a connection to an external electrical supply, through sharp contact pins or through bonded thin metal wires. When electrical current is passed through each thermal expansion beam, the Joule heating in each beam results in thermal expansion outward [Fig. 1(b)]. This expansion is translated to the moving platform by the V-shaped thin beam, whose ends are attached to the actuator. The translation factor r (amplification ratio) is a function of the angle θ between the axes of the slanted V-shaped beam and the thermal expansion beam ($r = \cot\theta$).[19] We chose the angle θ to be 5°, as recommended in the literature,[20,21] so the amplification ratio of the devices r was 11.

The symmetric V-beam minimizes the heat transfer from the actuator to the test sample in two ways. The temperature dependence of the strain in a heated beam is $\varepsilon = \alpha \Delta T$, where α is the thermal expansion coefficient ($2.6 \times 10^{-6}/°C$ for Si)[22] and ΔT is the change in temperature. For example, to achieve 260 nm displacement with a 1000 μm long Si thermal expansion beam, an increase of 100 °C is needed. With the V-beam used here ($r = 11$), for the same 260 nm displacement a temperature increase of only 9 °C is required. Secondly, when the outer two electrodes have the same potential, the symmetrical layout prevents current flow through the V-beam, so that resistive heating in the V-beam is avoided. In addition, our design transforms the compressive stress in the heated (thermal expansion) beams into tensile stress in the V-beam, thus preventing the possibility of buckling in the long and thin V-beam if large displacements are required. This layout, which has a flexible V-shaped beam, allows for expansion of the V-beam even for a very small temperature change in the thermal expansion beams, in contrast to other actuators that use a directly heated V-beam.[11,13]

For test samples that may be only microns or less in length, achieving a near-zero height difference (offset) between the fixed and moving platforms is critical. Thus, the freely suspended structures should not be easily displaced out of plane, and should have very close to zero offset prior to actuation. Typical surface-micromachined devices have a thickness of ~2 μm and are made out of polysilicon, which usually retains residual stress once deposited. This internal stress can easily bend a long beam in uncontrollable ways. The whole structure could also be bent out of plane by parasitic forces, such as capillary forces or via electrostatic coupling between the structural layer and the substrate. To avoid such undesirable factors, our device was machined out of 130 μm thick single crystal silicon. The large thickness of all of the beams (130 μm) ensures a large out of plane stiffness, such that it is possible to maintain a small vertical offset between the opposing platforms as discussed below.

The actuator was fabricated from silicon on glass made by anodic bonding. Figure 2 illustrates the fabrication process. A double-side polished 130 μm thick Si wafer was used for the device layer (3 in. diameter, Virginia Semiconductor, resistivity $<1\ \Omega$ cm) and a Borofloat® glass wafer (4 in., Mark Optics) was used as a substrate; both were cleaned using the RCA process.[23] The two cleaned wafers were brought into contact in an EV501 wafer bonder, and the temperature was increased to 350 °C while a bias of 1000 V was applied to form a permanent anodic bond at the interface of these two wafers. The device patterns were lithographically transferred to the surface of the device layer bonded to the substrate as shown in Fig. 2(a). The wafer was then etched with the Bosch DRIE process (both a PT770 Plasma Therm and a Unaxis 770 were used) with 3.5 μm photoresist (SPR220-3.0, Shipley) as the etch mask. The device-layer wafer was etched through, and etching stopped at the surface of the glass substrate as shown in Fig. 2(b). The photoresist was then removed either by Nanostrip (Cyantek) or O_2 plasma (Branson Barrel Etcher). A thin layer of Au was then deposited by thermal evaporation with 10 nm Cr as the ad-

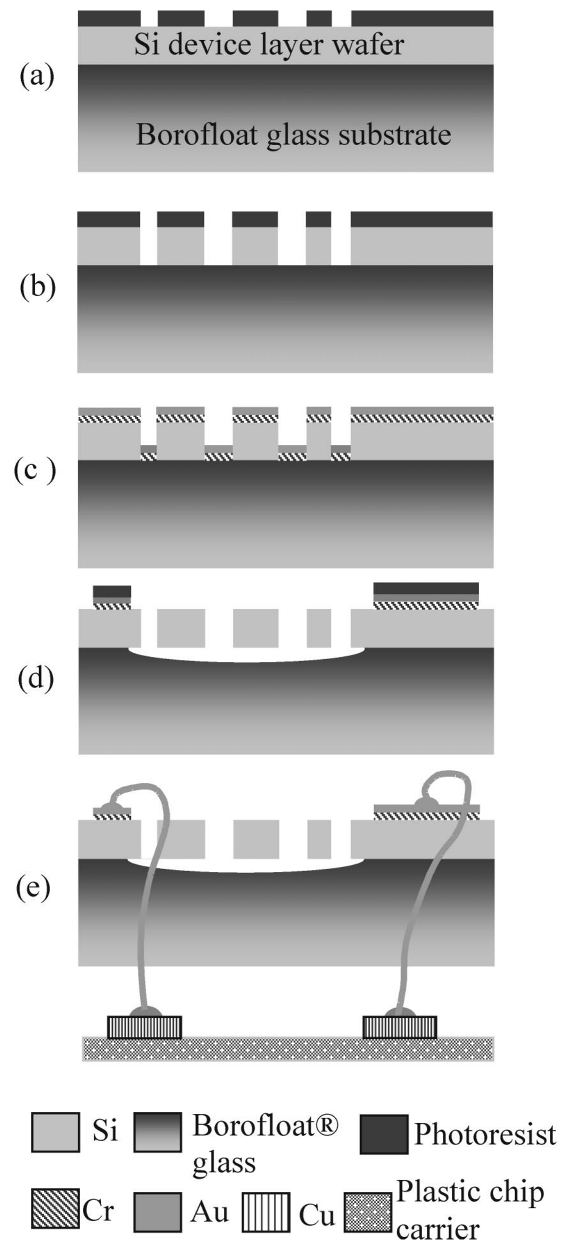

FIG. 2. The process sequence for the fabrication of the device: (a) Anodic bonding and photolithography of the top of the device layer wafer. (b) DRIE of device layer Si. (c) Photoresist removal followed by deposition of Cr and Au. (d) Electrical contact patterning of Cr and Au, and timed HF etching of glass. (e) Photoresist removal from the electrical contacts, and wires connecting the device to a chip carrier.

Downloaded 04 Jun 2004 to 129.105.90.23. Redistribution subject to AIP license or copyright, see http://rsi.aip.org/rsi/copyright.jsp

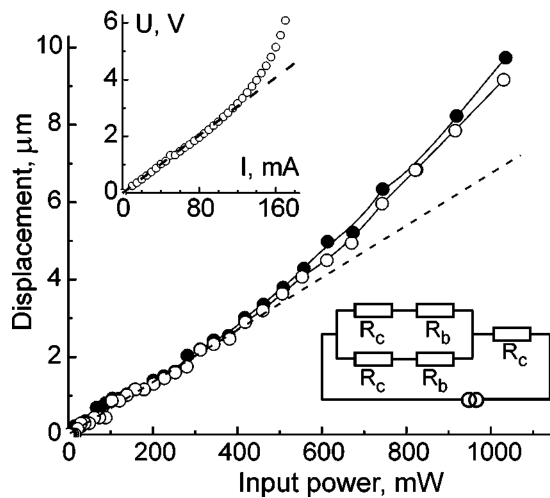

FIG. 3. Moving platform displacement (observed by a light microscope equipped with a CCD camera) as a function of total input power. The solid circles are the displacement with increasing power, and the open circles are displacement with decreasing power. The upper left-hand side inset is the voltage (V) vs current (I) dependence for the device during the test, which shows the nonlinear behavior of the resistance at a higher-power level, from ~ 120 mA. The lower right-hand side inset is the equivalent circuit of the system. R_c indicates the contact resistance, including the metal–Si interface and thin bonded wire, and R_b is the resistance of the Si beams.

hesion layer (SC4500 evaporator), as shown in Fig. 2(c). The metal electrodes were defined by covering each of the silicon electrodes with a drop of photoresist (S1818, Shipley). The photoresist was then soft baked and the chip was immersed in Au etchant (Type TFA, Transene Company) and followed by dipping into Cr etchant (Transene Company) for a few seconds each. Each device was then cut off the wafer. The structures were then released (to suspend the beams) by the timed etching (49% HF, Fisher Scientific) of the glass beneath them for each individual device, as shown in Fig. 2(d). Finally, the photoresist was cleaned with acetone and the metal pads were wire bonded (Kulicke & Soffa 4524 Digital) to a chip carrier to form the electrical connection to outer circuits as shown in Fig. 2(e).

III. CHARACTERIZATION OF THE DEVICE PERFORMANCE

The following procedure was used to test the relevant resistances of each MEMS device. The resistance for each of the two symmetrical pairs of thermal expansion beams $[1\&1', 2\&2'$, in Fig. 1(a), and R_b in Fig. 3] was 40 Ω, as measured with the four-probe method. From the known dimensions of the thermal expansion beams, the resistivity of the Si was determined to be $\sim 0.01\ \Omega$ cm. The total resistance of all tested devices was between 25 and 28 Ω. Each of the three metal Si contact together with the bonded Au wire [see Fig. 1(b)] had a resistance of 5 Ω. The power efficiency for our thermal actuator was determined to be $\sim 75\%$, with a power loss at the metal–Si interface of $\sim 25\%$. The interface pads (bilayer Cr/Au, as described above) are large (more than 1 mm^2 each) and are situated on top of wide Si pads; their heating is thus negligible compared to the actuator beams. The power efficiency and time response of the device depends on the ratio of R_b (thermal expansion beam resistance) to R_c (the contact resistance), and each could be improved by, for example reducing the width of the thermal expansion beams.

The device performance was characterized in three ways: (1) the displacement range was determined with light microscopy under ambient conditions, (2) the nanoscale displacement range was determined in a SEM under vacuum, and (3) the z offset (height difference) between the two platforms during operation was determined with optical profilometry under ambient conditions.

A. Displacement measurement

Here, we present characterization results obtained for two devices made during the same fabrication run (i.e., on the same wafer). The displacement of the moving platform was first investigated under a light microscope (MicroZoom, Bausch&Lomb) equipped with a charge coupled device (CCD) camera (HV-C20M, Hitachi) under ambient conditions. The current was monotonically increased or decreased as the voltage drop across the device was simultaneously recorded (HP6612C). Each device was tested several times, with each test involving several cycles of input power.

Figure 3 shows typical device performance versus input power. This device was tested over a large power input to determine its working range and the linearity of motion. The distance between the moving and fixed platforms was measured from the digital video recording and the displacement was obtained by subtracting the original gap distance. A large displacement range, from submicrometer to 9.7 μm was obtained for power input ranging from 0 to 1.04 W. This 9.7 μm displacement corresponds to a calculated force output of 88 μN from the actuator, translated by the V-beam, as discussed further below. As seen in Fig. 3, the displacement is essentially linear as a function of input power below 0.4 W.

The elongation of the thermal actuator and resulting platform motion is proportional to the input power, I^2R, where I is the input current and R is the electrical resistance of the heated beams. Theoretically, the resistance of the beam should be temperature dependent. We have studied this by plotting the current–voltage curve (Fig. 3, top inset); under ambient conditions, at input power below 0.36 W, the resistance is temperature independent; above this threshold, the resistance increases in a nonlinear fashion with respect to input power. It is estimated that at 0.36 W the temperature has increased 100 °C above room temperature. Such a high temperature could cause instability in the device by heating up the structures in the surrounding environment. Above this input power, instability in the measured offset was also observed. There is probably a connection between the temperature dependent resistance above 0.36 W and this instability, discussed below, in the measured offset.

Each device was further tested inside a LEO 1525 SEM at a vacuum of $\sim 10^{-4}$ Pa. Here, we used two methods to supply power to the actuator: A monotonic increase of current followed by a slow decrease (we refer to this as the ‘‘dc method’’), and, separately, periodic actuation with applied pulses of a rectangular shape (we refer to this as the ‘‘ac method’’). In both cases, the platform motion was observed via high-resolution SEM imaging. We note that motion con-

Downloaded 04 Jun 2004 to 129.105.90.23. Redistribution subject to AIP license or copyright, see http://rsi.aip.org/rsi/copyright.jsp

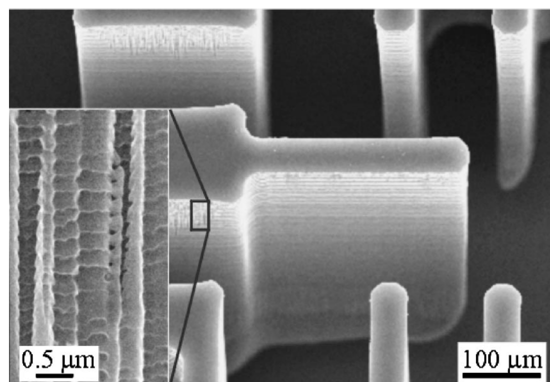

FIG. 4. An example of the scallop features on the sidewall of the DRIE-etched Si beam. Inset shows a portion of the side wall at higher magnification.

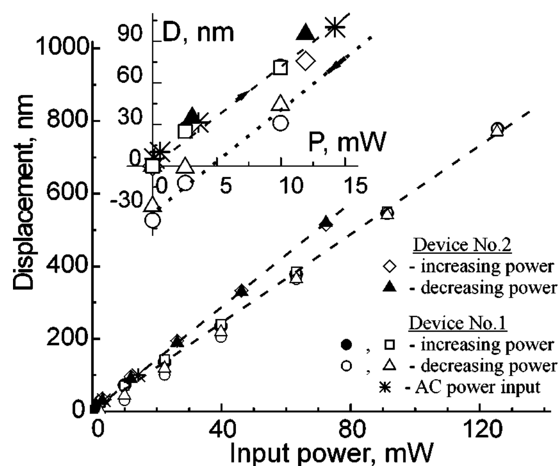

FIG. 5. The moving platform displacement vs total input power for two devices, measured in an SEM by the dc and the ac methods. The inset shows a plot at very small displacements; *D* is the displacement and *P* is the power input. All dashed lines are linear fits. The dotted line in the inset shows the displacements measured during the cool down process and the hysteresis between initial and final displacements due to SEM drift during the dc method measurement.

trol requiring *nanoresolution* cannot rely on approaches, such as those used for scratch drive actuators,[24,25] where the minimum displacement resolution is *calculated* by dividing a relatively large displacement by a certain signal count n. While capacitive sensing is a popular method for detecting motion in MEMS devices,[13] to sense displacements of a few nanometers would require a very large capacitor surface, which would greatly increase the total device size. As one of our goals is to develop a TEM-compatible nanotesting stage based on the current design, it is essential to minimize device size.

To observe nanometer-scale motion, we typically must work at 100 K–200 K SEM magnification. Since the top surface of the silicon is very smooth, it is hard to find a small and crisp object to track at such high magnification. In the future, it will be possible to deliberately ''decorate'' the top surface of the device so that motion could be more easily tracked. However, for the work reported here, we used the ''scalloped'' features on the side wall generated by the DRIE process as a tracking object. Figure 4 shows these features on the moving platform. Any straight vertical line on the surface can be used to track the platform displacement during an increment or decrement of applied power.

Figure 5 shows the displacement of the moving platform, versus power input applied by the dc method, for two devices in the low-power range. The change in position of the moving platform was measured from each steady-state position to the next one after applying a 10 mA increment in current. The total displacement was determined by summing these individual displacements. The displacement was linearly dependent on input power for both devices, but with a small difference in slope. We believe that this is caused by slightly different thermal equilibrium conditions for the two devices and small differences in thermal actuator resistance. The smallest measured displacement for both devices was 30 nm, at an input current of 10 mA. However, this is not a fundamental limit for either the displacement resolution or the input current, as confirmed using the ac method discussed below.

The use of SEM images to determine each displacement step is dependent on the absolute stability of the device and the lack of any drift of the microscope itself. Even small drifts in the microscope cause the object being tracked to move in the frame of reference of the SEM, but not necessarily with respect to the reference frame of the device. Unless drift can be eliminated or removed from the displacement calculation, the dc method will only be useful for relatively fast-loading experiments where the drift of the SEM is negligible (however, we note that image resolution is sacrificed when one uses a faster image capture mode with the SEM). The inset in Fig. 5 shows the displacement response of the devices at very low-power levels. Particularly for the long time and high-power inputs, when the power was returned to zero, the moving platform did not return to its initial position in the frame of reference of the SEM and hysteresis is observable in the response. This situation is unacceptable for high accuracy measurements and, for this reason, we also used an ac method to introduce periodic actuation as described below. As shown in the inset of Fig. 5, there is no hysteresis for the ac power-driven displacement (star symbol), suggesting that this method may be more suitable when high-resolution displacement control is required.

In Fig. 6(b), one sees a periodic appearance for each of the two scalloped edges shown in Fig. 6(a), which can (in principle) be restored by shifting the protruding sections in space. The periodic appearance is a consequence of the convolution of the ac actuation and the rastering of the electron beam over this area. The applied square-wave voltage is shown schematically in Fig. 6(c). The electrical current through the device was simultaneously measured to obtain the input power. The dc voltage offset was applied together with the ac input and was equal to one-half of a pulse amplitude, with the goal of achieving full cool down conditions for the device at each half-period (50% duty cycle). The images in Figs. 6(d)–6(h) demonstrate that the device responds faster (whether warming or cooling) than the scan speed of the electron beam, since the distorted edge ''simultaneously'' follows the rise and fall time of the applied ac voltage pulses. With the known e-beam rastering time, and

Downloaded 04 Jun 2004 to 129.105.90.23. Redistribution subject to AIP license or copyright, see http://rsi.aip.org/rsi/copyright.jsp

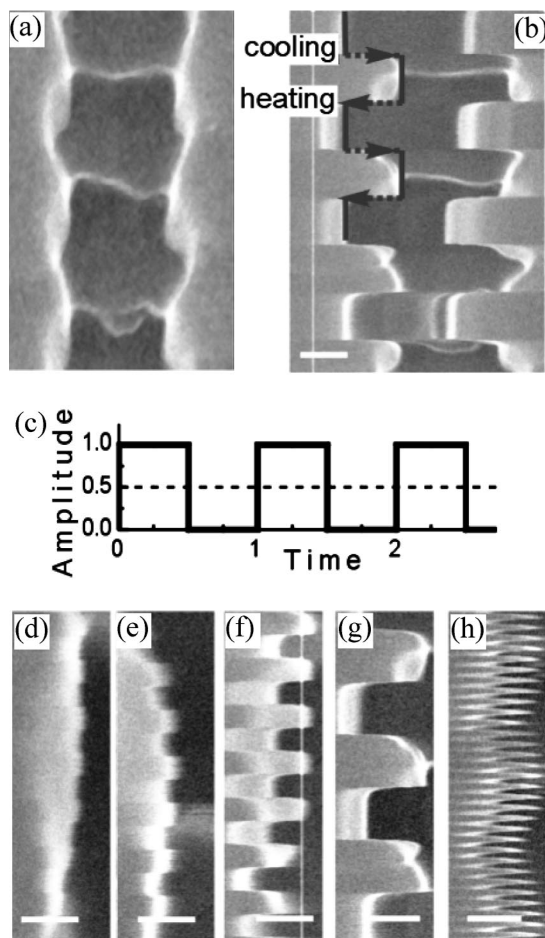

FIG. 6. The use of a slower scan mode to detect motion in the LEO 1525 SEM with a periodic power input to the thermal actuator. (a) The original shape of a scallop feature on the sidewall of the platform that moves. (b) The fragment of a SEM image taken at slow electron-beam scan mode (49.6 s per whole image) during the rectangular shape voltage pulses applied to the thermal actuator. (c) A schematic representation of these pulses. In (b), cooling and heating phases of the actuator are indicated by arrows (from the left- to the right-hand side is cooling, and from the right- to the left-hand side is heating). The fragments of SEM images of the scallop edge features at applied ac voltages: (d) $f=0.2$ Hz and $V_{p\text{-}p}=0.1$ V. Scale bar is 50 nm. Corresponding amplitude of the platform motion, $A=5\pm2$ nm. (e) $f=0.2$ Hz and $V_{p\text{-}p}=0.2$ V. Scale bar is 50 nm. $A=10\pm2$ nm. (f) $f=0.2$ Hz and $V_{p\text{-}p}=0.5$ V. Scale bar is 50 nm. $A=31\pm2$ nm. (g) $f=0.1$ Hz and $V_{p\text{-}p}=1$ V. Scale bar is 100 nm. $A=116\pm4$ nm. (h) $f=1$ Hz and $V_{p\text{-}p}=1$ V. Scale bar is 100 nm. $A=116\pm4$ nm.

the magnitude of the platform motion in response to ac pulses, we estimated the upper limit of the response time of our thermally actuated stage to be less than 1 ms. More detailed measurements will be reported in the future.

For the ac method operating at 0.1 Hz frequency of input power, ten warming–cooling periods occur in 1 s, whereas a typical full SEM image raster time can vary from ~10 to 90 s (we typically used ~30 to 40 s). Thus, the ac method employed here, or variants of it, will be useful for periodic loading of nanostructures for studies of such issues as fatigue, and for long time loading or unloading experiments, where elimination of the drift (in the frame of reference of the SEM, not the device itself) of the internal references discussed above is critically important. The main advantage of the ac method is thus that long-time drift in the SEM

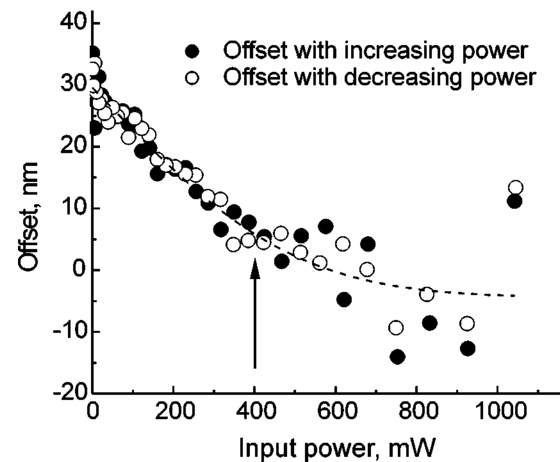

FIG. 7. Height difference between the moving and fixed platforms at different power inputs. The arrow indicates the onset of nonlinear behavior.

image is "removed" because of the oscillation between zero and maximum displacement. When dc power input is desired, it will be important to have internal reference marks from which to obtain the true displacement of the movable platform at the magnification used. For example, the device surface could be decorated with small particles and then, through imaging with a high-resolution microscope (such as a SEM, atomic force microscope, etc.), the relative displacement of the platform can be measured. Through fitting the dependence of displacement on input power, one can determine the smaller input powers needed to achieve smaller displacement. The limiting factors for small displacement control should be the stability of the power supply used and the electrical noise in the entire circuit; this will be further investigated in the future. Although we have, throughout this article, emphasized the more conservative estimate of 30 nm displacement, as shown in Fig. 6(e), it was possible to measure with the ac method displacements of 10 nm with an estimated error of ±2 nm. It is even possible to discern displacements of ~5 nm, see Fig. 6(d).

B. Offset measurement

Achieving a very small height offset between the two opposing platforms separated by the gap is critical for accurate mechanics measurements on nanoscale samples. The offset for the same two devices characterized above was examined in ambient conditions using an optical profilometer with 2.2 nm vertical resolution (MicroXAM, ADE Phase Shift Technology). The offset in height (z offset) was determined by constructing the topography [(x, y, and z) points] of the controlled gap region [Fig. 1(c)]. By comparing the z values of particular points of interest, the relative height difference between them could be obtained. The z offset at a series of displacement values of the moving platform was measured in ambient and at each steady state to determine the dependence of offset on platform displacement. The device was again actuated with a monotonic increase and then decrease of the current (dc method) as described above. The measured z offset versus input power is shown in Fig. 7. As both input power and displacement of the actuated platform

Downloaded 04 Jun 2004 to 129.105.90.23. Redistribution subject to AIP license or copyright, see http://rsi.aip.org/rsi/copyright.jsp

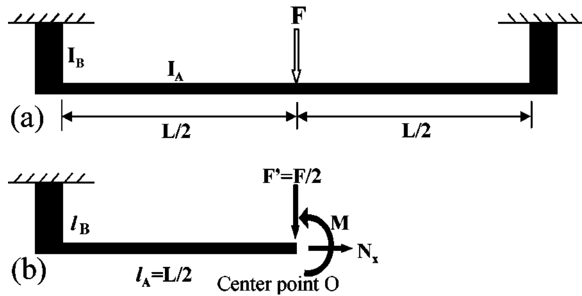

FIG. 8. (a) Schematic of bending the force-sensing beam (top view of the device). (b) Force analysis on half of the beam.

increased, the offset decreased from 35 nm to ~5 nm. It is thought that the thermal expansion of the actuator not only pushed the structure laterally, but also lifted it a small amount because of internal stresses in the Si. However, as shown in Fig. 7, in the high-power range (above approximately 400 mW) the devices showed an increasing instability in the offset compared to the low input power response. This also suggests that the rise in device temperature at an input power above ~400 mW causes unstable device operation as was observed in Fig. 3.

C. Theoretical analysis of force output

With the input of a given electrical power, the V-beam and the coupled force-sensing beams deform continuously until equilibrium is reached. At equilibrium, the force output of the actuator is equal to the force needed to bend the force-sensing beam, and the amount of bending corresponds to the displacement of the moving platform, as shown in Fig. 1(a). With the measured displacement of the moving platform as an input, simple beam theory can be used to determine the output force of the actuator.

Since both the V-beam and the force-sensing beam have large out-of-plane stiffnesses (557 N/m for a 6 μm wide, 130 μm deep, and 1000 μm long beam), the out-of-plane displacement is neglected and plane-strain conditions are assumed. The force-sensing beam is clamped at its two ends as shown in Fig. 8(a). We denote F as the force applied by the actuator. Due to the symmetry of the structure, only half of the structure is analyzed, and the force $F' = F/2$ as shown in Fig. 8(b). Besides the force applied by the actuator, the half-beam is subjected to a horizontal force, N_x, and a moment, M. Within the framework of linear elasticity, the displacements of the symmetry plane are linearly dependent on the applied forces,

$$\alpha_o = \frac{1}{2EI_B}\ell_B^2 N_x + \left(\frac{1}{EI_A}\ell_A + \frac{1}{EI_B}\ell_B\right)M - \left(\frac{1}{2EI_A}\ell_A^2 + \frac{1}{EI_B}\ell_A\ell_B\right)F', \tag{1}$$

$$\Delta x_o = \frac{1}{3EI_B}\ell_B^3 N_x + \frac{1}{2EI_B}\ell_B^2 M - \frac{1}{2EI_B}\ell_A\ell_B^2 F', \tag{2}$$

$$\Delta y_o = -\frac{1}{2EI_B}\ell_A\ell_B^2 N_x - \left(\frac{1}{2EI_A}\ell_A^2 + \frac{1}{EI_B}\ell_A\ell_B\right)M - \left(\frac{1}{3EI_A}\ell_A^3 + \frac{1}{EI_B}\ell_A^2\ell_B\right)F', \tag{3}$$

where α_0 is the angle of bending at the tip of the half beam, I_A and I_B are the moment of inertia of the half beam and the short beam, ℓ indicates the length of the beam, and Δx_0 and Δy_0 are the horizontal and vertical displacements at the end of the half-beam, respectively.

Using the symmetry conditions of vanishing α_0 and Δx_0, the above equations yield a linear relation between the deflection of the beam and applied force,

$$\Delta y_o = CF, \tag{4}$$

where C is the effective compliance of the structure and can be written as

$$C = \frac{1}{2}\left(\frac{1}{3EI_A}\ell_A^3 + \frac{1}{EI_B}\ell_A^2\ell_B\right) - \frac{3}{4EI_B}\ell_A^2\ell_B\left(\frac{\ell_A I_B + \ell_B I_A}{4\ell_A I_B + \ell_B I_A}\right) - \frac{1}{2}\left(\frac{2I_B\ell_A^2 - \ell_A\ell_B I_A}{4\ell_A I_B + \ell_B I_A}\right)\left(\frac{1}{2EI_A}\ell_A^2 + \frac{1}{EI_B}\ell_A\ell_B\right). \tag{5}$$

In the limiting case when $I_B \gg I_A$, the effective compliance becomes

$$C = \frac{\ell_A^3}{24EI_A}. \tag{6}$$

Using the current device dimensions, the device compliance from Eq. (5) is 0.1106 m/N and from Eq. (6) 0.105 m/N; the difference between these two solutions is 5%. For the maximum midpoint displacement of 9.7 μm as measured by the light microsope CCD system, the force obtained from Eq. (5) was 87.7 μN. For the minimum 30 nm displacement measured in SEM, the force obtained is 0.27 μN. The structure was also analyzed by finite-element calculations using the commerical package ANSYS 5.7, from which we obtained a spring constant of 8.74 N/m, which differs by less than 5% from the analytical solution given in Eq. (5).

IV. USE AS A TESTING DEVICE

By obtaining the difference in displacements of the movable platform with and without the nanostructure for a particular input power, the stiffness constant of the nanostructure can be obtained as shown schematically in Fig. 9. For the particular design presented here with a 20 μm initial gap, the minimum displacement measured with the dc method is 30 nm, such that we can load a test specimen at strain larger than 0.15%. Given this displacment, our analysis shows that the force applied to the test sample can be between 0 and ~22.4 μN (the stable working range of the device up to 0.36 W power input due to the height offset). The minimum applied force is determined by the resolution of the displacement measurement; for example, for a displacement resolution of 5 nm, the minimum force resolution is 45 nN

Downloaded 04 Jun 2004 to 129.105.90.23. Redistribution subject to AIP license or copyright, see http://rsi.aip.org/rsi/copyright.jsp

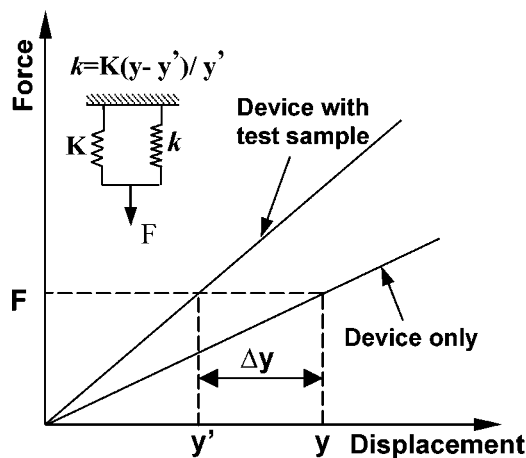

FIG. 9. A schematic of how to measure the stiffness of a test sample using the device: With known power, the displacement is measured before (y) and after loading a specimen (y'); a given power corresponds to a given force output. The sample stiffness is in parallel with the force-sensing stiffness, thus $F=Ky=(K+k)y'$. Thus, the spring constant of the sample, k, is $k=K(y-y')/y'$, where K is the spring constant of the force-sensing beam.

(corresponding to 40 nm displacement before material loaded and 35 nm minimum displacement with material loaded). The maximum force that would be applied on the material at this displacement is 22 μN.

The range of moduli values that can be measured in this force range and at this displacement for a particular material can be estimated given a particular cross-sectional area; for example, for a nanorod with 150 nm diameter, moduli between 1.45 GPa and 0.7 TPa (and tensile strengths between 2.56 MPa and 1.24 GPa) can be obtained. However, for extremely stiff materials and structures with small cross-sectional areas, while the range of forces of the device are sufficient, the resolution of the elongation measurement of the sample will limit the utility of a *particular loading device* as a loading stage for a *particular* material. For example, we consider a (10,10) SWCNT with a gauge length of 20 μm that breaks at an assumed 10% strain with an assumed value for the applied force of $\sim$150 nN at break. The thermal actuator can provide the necessary tensile force which would result in a $\sim$2 μm displacement of the moving platform. Because the force is distributed between both the specimen (the SWCNT) and the force-sensing beam, a larger overall force ($\sim$18.2 μN) is required, see Fig. 9. As mentioned above, the upper limit of the linear working range (but determined without a specimen clamped between stationary and moving platform) is $\sim$22 μN; it is possible that the linear working range will extend to significantly higher values when a specimen physically links the moving to the stationary platform. So, this device may barely be able to load a defect-free SWCNT to the break point. Also, the distribution of a very large fraction of the overall force to the force-sensing beam is a limitation of the current design, for measurements on such a small sample. Fortunately, modifications to overcome several minor limitations of this stage, are straightforward.

We plan on incorporating changes in design to: (a) Decrease the gap size to 1 micron; this is a conservative estimate, we believe we can achieve smaller gaps by several different methods, (b) enhance the displacement resolution, (c) introduce direct force sensing methods, such as a cantilever whose displacement can directly be used to measure the applied force. Finally, we note that the design and fabrication methodology as described above can be easily adjusted to produce a variety of custom-designed devices each having a desired range of force and displacement, and needed resolution in each, suitable for a variety of sample types.

In summary, a thermally actuated testing stage with controlled displacement for mechanics measurements of nanostructures and thin films was designed and fabricated using MEMS technology. The temperature rise necessary to actuate this device is minimized through use of a V-beam amplification structure, and its symmetric design. The height offset between opposing platforms was measured to be less than 40 nm over the full working range (to 9.7 μm displacement). In addition, a new method of measuring nanometer scale displacement using ac-based thermal actuation within a SEM was developed. The minimum displacement measured with a dc input signal was 30 nm in a vacuum; a displacement of only 5 ± 2 nm was observed using an ac signal. The stable working range of the device with no sample present is up to $\sim$2.5 μm displacement, and the calculated actuator force over this range is from 0 to $\sim$22.4 μN. The excellent offset between the separated platforms during actuation, the small operating temperatures, the linear response (displacement versus input power), and the large stable working range show that the design approach and methodology are sound and can now be used to produce a variety of stages for different ranges of input force and displacement resolution.

ACKNOWLEDGMENTS

The authors gratefully acknowledge the Office of Naval Research *Mechanics of Nanostructures* grant (Award No. N000140210870), and the NASA University Research, Engineering, and Technology Institute on Bio Inspired Materials (BIMat) under Award No. NCC-1-02037. Scanning electron microscopy testing was done at the Electron Probe Instrumentation Center at Northwestern University. The fabrication work was performed in part at the Cornell Nano-Scale Science and Technology Facility (a member of the National Nanofabrication Users Network), which is supported by the National Science Foundation under Grant No. ECS-9731293, its users, Cornell University, and Industrial Affiliates. The authors appreciate assistance in the fabrication from Will McBride and comments by Kevin Kohlhaas.

[1] M. F. Yu, B. S. Files, S. Arepalli, and R. S. Ruoff, Phys. Rev. Lett. **84**, 5552 (2000).
[2] M. F. Yu, M. J. Dyer, G. D. Skidmore, H. W. Rohrs, X. K. Lu, K. D. Ausman, J. R. Von Ehr, and R. S. Ruoff, Nanotechnology **10**, 244 (1999).
[3] M. F. Yu, O. Lourie, M. J. Dyer, K. Moloni, T. F. Kelly, and R. S. Ruoff, Science **287**, 637 (2000).
[4] M. F. Yu, B. I. Yakobson, and R. S. Ruoff, J. Phys. Chem. B **104**, 8764 (2000).
[5] Z. W. Pan, S. S. Xie, L. Lu, B. H. Chang, L. F. Sun, W. Y. Zhou, G. Wang, and D. L. Zhang, Appl. Phys. Lett. **74**, 3152 (1999).
[6] J. J. Yao, S. C. Arney, and N. C. MacDonald, J. Microelectromech. Syst. **1**, 14 (1992).

Downloaded 04 Jun 2004 to 129.105.90.23. Redistribution subject to AIP license or copyright, see http://rsi.aip.org/rsi/copyright.jsp

[7] J. Brugger, V. P. Jaecklin, C. Linder, N. Blanc, P. F. Indermuhle, and N. F. de Rooij, J. Micromech. Microeng. **3**, 161 (1993).
[8] N. D. Mankame and G. K. Ananthasuresh, J. Micromech. Microeng. **11**, 452 (2001).
[9] P. A. Williams, S. J. Papadakis, M. R. Falvo, A. M. Patel, M. Sinclair, A. Seeger, A. Helser, R. M. Taylor, S. Washburn, and R. Superfine, Appl. Phys. Lett. **80**, 2574 (2002).
[10] G. G. Demczyk, Y. M. Wang, J. Cumings, M. Hetman, W. Han, A. Zettl, and R. O. Ritchie, Mater. Sci. Eng., A **334**, 173 (2002).
[11] E. H. Klaassen, K. E. Petersen, J. M. Noworolski, J. R. Logan, N. I. Maluf, J. Brown, C. Storment, W. McCulley, and G. T. A. Kovacs, *Proceedings of the Eighth International Conference on Solid-State Sensors and Actuators and Eurosensors IX: Digest of Technical Papers* (IEEE, Stockholm, 1995), pp. 556–559.
[12] M.-F. Wu, C.-H. C. Lin, and W. Hsu, J. Intell. Mater. Syst. Struct. **10**, 402 (1999).
[13] L. L. Chu and Y. B. Gianchandani, J. Micromech. Microeng. **13**, 279 (2003).
[14] E. S. Kolesar, P. B. Allen, J. T. Howard, and J. M. Wilken, J. Vac. Sci. Technol. A **17**, 2257 (1999).
[15] R. R. A. Syms, J. Micromech. Microeng. **12**, 211 (2002).
[16] D. M. Burns and V. M. Bright, SPIE Int. Soc. Opt. Eng. **3224**, 296 (1997).
[17] J. H. Comotois and V. M. Bright, Sens. Actuators, A **58**, 19 (1997).
[18] T. Moulton and G. K. Ananthasuresh, Sens. Actuators, A **90**, 38 (2001).
[19] N. Takeshima, K. J. Gabriel, M. Ozaki, J. Takahashi, H. Horiguchi, and H. Fujita, Transducers' 91: *International Conference on Solid-State Sensors and Actuators* (IEEE, San Francisco, 1991), pp. 63–66.
[20] Y. B. Gianchandani and K. Najafi, J. Microelectromech. Syst. **5**, 52 (1996).
[21] L. Que, J.-S. Park, and Y. B. Gianchandani, J. Microelectromech. Syst. **10**, 247 (2001).
[22] Y. Okada and Y. Tokumaru, J. Appl. Phys. **56**, 314 (1984).
[23] M. J. Madou, *Fundamentals of Microfabricaton* (CRC Press, Boca Raton, 1997).
[24] L. Y. Lin, J. L. Shen, S. S. Lee, and M. C. Wu, IEEE Photonics Technol. Lett. **9**, 345 (1997).
[25] R. J. Linderman and V. M. Bright, Sens. Actuators, A **91**, 292 (2001).

Downloaded 04 Jun 2004 to 129.105.90.23. Redistribution subject to AIP license or copyright, see http://rsi.aip.org/rsi/copyright.jsp